PLOS COMPUTATIONAL BIOLOGY

RESEARCH ARTICLE

A combined experimental-computational approach uncovers a role for the Golgi matrix protein Giantin in breast cancer progression

Salim Ghannoum[1‡*], Damiano Fantini[2‡], Muhammad Zahoor[1], Veronika Reiterer[3], Santosh Phuyal[1], Waldir Leoncio Netto[4], Øystein Sørensen[5], Arvind Iyer[6], Debarka Sengupta[7,8], Lina Prasmickaite[9], Gunhild Mari Mælandsmo[9,10], Alvaro Köhn-Luque[4*], Hesso Farhan[1,3*]

1 Institute of Basic Medical Sciences, Department of Molecular Medicine, University of Oslo, Oslo, Norway, **2** Department of Urology, Northwestern University, Chicago, Illinois, United States of America, **3** Institute of Pathophysiology, Medical University of Innsbruck, Innsbruck, Austria, **4** Oslo Centre for Biostatistics and Epidemiology, Faculty of Medicine, University of Oslo, Oslo, Norway, **5** Center for Lifespan Changes in Brain and Cognition, Department of Psychology, University of Oslo, Oslo, Norway, **6** Department of Computational Biology, University of Lausanne (UNIL), Lausanne, Switzerland, **7** Department of Computational Biology, Indraprastha Institute of Information Technology, New Delhi, India, **8** Centre for Artificial Intelligence, Indraprastha Institute of Information Technology, Delhi, India, **9** Department of Tumor Biology, Institute for Cancer Research, Oslo University Hospital, The Norwegian Radium Hospital, Oslo, Norway, **10** Department of Medical Biology, UiT—The Arctic University of Norway, Tromsø, Norway

‡ These authors share first authorship on this work.
* salim.ghannoum@medisin.uio.no (SG); alvaro.kohn-luque@medisin.uio.no (AKL); hesso.farhan@i-med.ac.at (HF)

Citation: Ghannoum S, Fantini D, Zahoor M, Reiterer V, Phuyal S, Leoncio Netto W, et al. (2023) A combined experimental-computational approach uncovers a role for the Golgi matrix protein Giantin in breast cancer progression. PLoS Comput Biol 19(4): e1010995. https://doi.org/10.1371/journal.pcbi.1010995

Editor: Roeland M.H. Merks, Leiden University Faculty of Science: Universiteit Leiden Faculteit der Wiskunde en Natuurwetenschappen, NETHERLANDS

Received: May 31, 2022

Accepted: March 4, 2023

Published: April 17, 2023

Data Availability Statement: The R code for the cancer simulator used in manuscript are deposited in Github: https://github.com/ocbe-uio/Cancer_simulator. All other relevant data are within the manuscript and its Supporting Information files.

Funding: HF is supported by funding from the Norwegian Cancer Society (grants 182815 & 208015), by the Norwegian Research Council

Abstract

Our understanding of how speed and persistence of cell migration affects the growth rate and size of tumors remains incomplete. To address this, we developed a mathematical model wherein cells migrate in two-dimensional space, divide, die or intravasate into the vasculature. Exploring a wide range of speed and persistence combinations, we find that tumor growth positively correlates with increasing speed and higher persistence. As a biologically relevant example, we focused on Golgi fragmentation, a phenomenon often linked to alterations of cell migration. Golgi fragmentation was induced by depletion of Giantin, a Golgi matrix protein, the downregulation of which correlates with poor patient survival. Applying the experimentally obtained migration and invasion traits of Giantin depleted breast cancer cells to our mathematical model, we predict that loss of Giantin increases the number of intravasating cells. This prediction was validated, by showing that circulating tumor cells express significantly less Giantin than primary tumor cells. Altogether, our computational model identifies cell migration traits that regulate tumor progression and uncovers a role of Giantin in breast cancer progression.

Author summary

The Golgi is a specialised structure inside cells that functions as a factory where molecules necessary for diverse cell functions are modified and sorted for transport. One of the

(grant 302452), by the Anders Jahre Foundation, and by the Rakel og Otto Kristian Bruun's Legat and by a grant from the Austrian Science Foundation FWF (P 358320). A.K.L is supported by the center for research-based-innovation BigInsight funded by the Research Council of Norway (grant number 237718), by the Research Council of Norway (grant 311188) and by the European Union's Horizon 2020 Research and Innovation Programme under Grant Agreement No. 847912. A.K.L and S.G were supported by the UiO:Life Science convergent environment PerCaThe. The funders had no role in study design, data collection and analysis, decision to publish, or preparation of the manuscript.

Competing interests: I have read the journal's policy and the authors of this manuscript have the following competing interests: D.F. is an employee of Xilio Therapeutics and a former employee and a shareholder of Eli Lilly and Company. The other authors declare that they have no competing interests.

proteins that maintains the physical structure of the Golgi is called Giantin. We found that breast cancer patients whose tumors have lower Giantin die earlier compared to patients with higher Giantin tumors. To find an explanation, we induced Golgi fragmentation in breast cancer cells by depleting Giantin. Interestingly, we found that Giantin depletion alters the migratory and invasive properties of those cells. To understand the implications of altered migration and invasion, we run computer simulation of tumor growth and progression with and without Giantin depletion. Our simulations predicted that Giantin-depleted tumors, while smaller, are nevertheless capable of seeding more cells inside the circulatory system. This is a precondition for the formation of metastases in distant organs, which is the major factor that determines mortality in breast cancer patients. To validate our model prediction, we showed that breast cancer cells that have enter the circulatory system have lower Giantin that the tumors in the breast where the cancer was originated. In summary, our combination of modeling and experimental validation provides a possible explanation for poor survival of breast cancer patients with low Giantin levels.

1. Introduction

Breast cancer is the most commonly occurring cancer in women and the fifth most common cause of cancer-related death [1,2]. The formation of metastases due to the spread of tumor cells to distant organs, is the major factor that determines mortality in breast cancer patients [3,4]. Metastatic dissemination of breast cancer cells is a multi-step process requiring the acquisition of a motile phenotype, the ability to invade the surrounding tissue, break into vessels and eventually extravasate and colonize distant organs [5]. Major research efforts in the past decades led to a firm understanding of the role of cell division, apoptosis and invasion in tumor progression and metastatic dissemination. However, there is surprisingly little knowledge of whether and how tumorigenesis is affected by different migration traits such as speed and directional persistence, *i.e.* the tendency to keep or change the direction of motion. Furthermore, the differential contribution of cell migration and invasiveness to the ability of cancer cells to escape from the primary tumor remains elusive.

The Golgi apparatus (hereafter referred to as the Golgi) is a major cellular organelle that is involved in the regulation of membrane trafficking and post-translational modifications. In addition, the Golgi plays an important role as a regulator of directional cell migration [6–8]. Under normal conditions, the Golgi is an intact single-copy organelle comprised of stacks of flattened cisternal membranes that are laterally linked to form the Golgi ribbon. This structure is maintained by Golgi-matrix proteins. Giantin is a such a Golgi-matrix protein that was shown to be important for maintaining the structural integrity of the Golgi [9–12]. Several alterations in cultured cancer cells were reported to result in fragmentation of the Golgi (reviewed in [13]). Moreover, RNAi screening approaches have identified a wide range of conditions that affect the morphology of the Golgi [14–17]. Golgi fragmentation has been reported to cause defects in cell polarization and therefore a delay in cell migration in wound closure assays [6,8,18]. Our previous work indicates that loss of a Golgi matrix protein GM130 in breast cancer cell lines is associated with altered migration and invasion [18]. However, this analysis was so far only performed in cell lines and a confirmation of the pathophysiological significance of Golgi fragmentation in patient samples remains to be shown. Moreover, it does not answer the fundamental question of how cell migration affects tumor progression, a relationship that remains incompletely understood. For instance, increasing cell turnover was

found to augment the effect of cell migration of tumor evolution [19]. The presence of cells moving in opposite directions (so called oncostreams) correlates with tumor growth [20,21]. However, how the combination of speed and persistence alters tumor growth is not well characterized.

In the present study, we used *in silico* simulations to analyze the impact of a wide range of speed-persistence combinations of the shape and size of tumors and on intravasation of cancer cells. To this end, we constructed a mathematical model that accounts for migration, proliferation, invasion and death of cancer cells in a two-dimensional space. This model predicted that speed and persistence are positively correlated with the growth of the primary tumor. We then fed experimental measurements of cell migration and invasion into our model to study the impact of Giantin depletion on tumor progression. The model predicted that Giantin-depleted tumors, while smaller, are nevertheless capable of seeding more intravasating cells. This conclusion was then substantiated by showing that circulating tumor cells have lower Giantin levels than primary tumor cells. Our combination of modeling and experimental validation provides a possible explanation for the poor survival of breast cancer patients with low Giantin levels.

2. Materials and methods

2.1. Cell culture and transfection

MDA-MB-231 and BT549 were cultured in RPMI supplemented with 10% FCS and 1% penicillin/streptomycin (GIBCO). Cells were transduced with NucLight green lentivirus (Essen BioScience, 4624). Infections were carried out using a multiplicity of infection (MOI) of three transducing units per cell. The growth medium was changed after 24h of transduction and cells were split after 72h. The transduced cells were sorted via fluorescence-activated cell sorting (FACS) using a BD FACSAria cell sorter. Sorted cells were tested for mycoplasma. For Giantin *(*GOLGB1) knockdown experiments, BT549 cells in optimal growth phase expressing GFP localizes to the nucleus were semireverse-transfected with siGENOME SMARTpool GOLGB1-siRNA (Dharmacon) with a final concentration of 15nM using HiPerfect (Qiagen, 301704) according to the manufacturer's instructions. The SMARTpool of GOLGB1-siRNA contains 4 individual siRNAs with the following sequences; GAACUAGAGUCUCGGUAUA, UAAGAAUUGCAACCUAA, GUACACAGGUUAAGUGCUU and GAAGGUCUGUGAU ACUCUA. The level of Giantin expression was determined by qRT-PCR. Total RNA was extracted using a GenElute Mammalian Total RNA Miniprep Kit (Merck, RTN70), and cDNA was reverse-transcribed using a High Capacity cDNA Reverse Transcription Kit (Thermo Fisher Scientific, Cat # 4368814). The expression of Giantin was determined using SensiFAST SYBR Hi-ROX (NordicBio, BIO-92002) and normalized to ACTIN using commercially available primers (Qiagen; for Giantin, QT00038087 and TBP, QT00000721).

2.2. Confocal immunofluorescence microscopy

GFP-BT549 cells were grown on glass cover-slips placed in a 6-well plate, and then fixed with 3% paraformaldehyde for 20 min at RT. Afterward, cells were washed in PBS with 20 mM glycine followed by incubation for 5 min at RT in permeabilization buffer containing PBS with 0.2% triton X100. Then, the fixed cells were incubated with mouse monoclonal anti-GM130 antibody (BD-Biosciences/Puls Medical, 610823) dilution 1:1000. After incubation with primary Abs at 37˚C for 1 h followed by washing with PBS three times, cells were incubated for another 1h in goat anti-mouse secondary antibody, Alexa Fluro 488 (Thermo Fisher Scientific, A-11001) diluted in 3% BSA in PBS. Finally, cells were mounted in polyvinyl alcohol with DABCO antifade and imaged. Imaging was performed on Zeiss LSM700 laser scanning

confocal microscope. All images were acquired randomly using a Plan- Aphochromat 63x Oil Ph3 M27 objective (NA 1.4).

2.3. Two-dimensional dense random migration assay

For optimal tracking efficiency we generated 3 populations; BT549 + GFP-BT549, BT549 + Giantin-silenced GFP-BT549, and MDA_MB_231 + GFP-MDA_MB_231. These cells were co-cultured at a ratio of 3:1 respectively in 96 well image-lock plates (EssenBio, 4739, Lot#17040501) for 24 hours at 37˚C and 5% CO_2. Then cells were scanned at ten-minute intervals over 24h in Essen BioScience's IncuCyte S3 with objective lenses 10x (NA; 0.95; Image Resolution: 1.24um/pixel) using both the phase channel (HD Phase imaging in gray values) and green channel (Emission Wavelength: 524nm; Excitation Wavelength: 460nm; Exposure Time: 200ms). Images were collected using a Basler Ace 1920-155um camera with CMOS sensor. Cellular viability was assessed throughout the course of the scanning by comparing the phase cellular morphology between mother cells and their corresponding GFP cells. ImageJ was used to linearly correct the brightness and contrast of the images and merging them as multi-TIFF stack. All the images collected from the same experiment were modified the same way to leave the information unaltered. GFP cells were tracked and subjected to trajectory analysis using the in-house developed *cellmigRation* package as described in the next section [22].

2.4. The *cellmigRation* package

The *cellmigRation* is an open-source R package that we developed to analyze cell movements using TIFF images captured over time. Its latest stable version is hosted on the peer-reviewed R Bioconductor repository for easy installation and usage (DOI: 10.18129/B9.bioc.cellmigRation). The software includes two modules aimed at *i)* data import and pre-processing; and *ii)* advanced analytics and visualization. Image pre-processing (Module 1) is performed similar to what described by *DuChez B*, 2018 [23]. Briefly, we ported the *FastTracks* software (https://www.mathworks.com/matlabcentral/fileexchange/60349-fasttracks) from *MATLAB* to R and added functionality to automate some of the initial optimization steps (background correction, signal detection). Similar to *FastTracks*, our R package can import TIFF files, perform background removal, detect signal peaks corresponding to fluorescent particles in each stack of the image and record the corresponding centroid coordinates. Next, cell trajectories are computed by connecting the closest centroids from consecutive stacks provided that they are located within a user-defined maximum displacement radius. Cell tracking data can be used as input for the advanced analytic and deep trajectory analysis functions (Module 2). Our software can compute several metrics and statistics. Specifically, *cellmigRation* includes functions dedicated to the analysis of *i)* cell persistence and speed; *ii)* directionality; *iii)* mean squared displacement; *iv)* direction auto-correlation; and *v)* velocity auto-correlation. Module 2 also includes functions aimed at exporting data, automatically building cell-based and population-based visualizations and generating 3D interactive plots. Cell trajectory Principal Component Analysis (PCA) and Clustering are supported as well.

2.5. Gelatin degradation assay

Sterile cover-slips (12 mm, #1 Menzel Microscope Coverslips) were coated with a thin layer of 0.2 mg/ml Oregon Green 488-gelatin (Life Technologies, G13186) for 20 min, fixed in 0.5% glutaraldehyde for 40 min and washed three times with sterile PBS. Cover-slips were then transferred to a 24-well plate and incubated in complete growth medium for 30 min at 37˚C. BT549 cells transfected with either Ctrl-siRNA or GOLGB1-siRNA (Dharmacon) for 48h were

seeded on top of the cover-slip at a density of $7.5x10^4$ cells/well and incubated overnight. Cells were then processed for anti-GM130 immunofluorescence staining. Images were randomly acquired on Andor Dragonfly spinning disk using a Nikon Ti2 inverted optical microscope equipped with a 60 × TIRF objective (Plan-APOCHROMAT 60 × /1.49 Oil). Fluorescence was collected using an EMCCD camera (iXon Ultra 888, Andor). To quantify the gelatin degraded areas per image, appropriate functions of ImageJ were used. The measured area was divided by the number of cells in the corresponding image. Kruskal-Wallis rank sum test was used to compare the gelatin degraded areas between the two conditions.

2.6. Patient-derived breast cancer xenografts

Patient-derived xenografts (PDX) were established at Institute for Cancer Research, Oslo University Hospital (MAS98.12 and MAS98.06) or the Institute Curie, France (HBCx-34 and HBCx-39) as previously described [24,25]. Briefly, primary mammary tumor specimens were implanted into immunodeficient mice. After initial establishment, the tumor tissue was serially transplanted into mammary fat pads of nude athymic mice. Based on histopatological and molecular characterization, the tumors were classified as triple-negative basal like (MAS98.12 and HBCx-39) and hormone receptors positive luminal B breast cancer (MAS98.06 and HBCx-34) [24,26,27]. our μm thick paraffin sections were rehydrated in a serial dilation of ethanol and boiled in TRIS-EDTA (pH 9.0) for antigen retrieval. The tissue sections were permeabilized with triton X-100 and then incubated at RT for 2 hours with anti-Giantin antibody (Nordic BioSite, bs-13356) dilution 1:1000. Then the tissue sections were washed with PBS three times, cells were incubated for another 1h in goat anti-mouse secondary antibody, Alexa Fluro 488 (Thermo Fisher Scientific, A-11001). The sections were incubated with Hoechst 33342 dye (Thermo Fisher Scientific, H3570) to stain the nuclei. The sections were rinsed with Milli-Q water and embedded in polyvinyl alcohol mounting medium (Sigma Aldrich, 10981). Fluorescence images were randomly acquired on on Andor Dragonfly spinning disk using a Nikon Ti2 inverted optical microscope equipped with a 60×TIRF objective (Plan-APOCHROMAT 60× /1.49 Oil). Fluorescence was collected using an EMCCD camera (iXon Ultra 888, Andor). To quantify the Golgi state, Golgi structure was assessed by visual inspection and categorized as intact, fragmented or undetermined.

2.7. Breast tissue array

Invasive ductal carcinoma and adjacent normal breast tissue samples were obtained from US Biomax, BC08118a. The slide was baked at 60˚C for 2h followed by incubation in Neo-clear (Sigma 109843) for 5min. The slide was re-hydrated in serial dilutions of Ethanol and then boiled in Tris/EDTA (pH 9,0) for 15min. After washing with PBS for 5min the slide was permeabilized using triton X-100 (0,25%) for 8min and then blocked in 5% BSA (in PBST) for 1h at RT. To stain the Golgi, the slide was incubated with anti-Giantin antibody (Nordic BioSite, bs-13356) in 1% BSA (PBST) for 2h at RT. After three times washing with PBST for 5min the slide was incubated for another 1h in goat anti-mouse secondary antibody, Alexa Fluro 488 (Thermo Fisher Scientific, A-11001). After several washing steps, the Hoechst 33342 dye (Thermo Fisher Scientific, H3570) was used to label the nuclei. Finally, the slide was rinsed with Milli-Q water and embedded in polyvinyl alcohol mounting medium (Sigma Aldrich, 10981). The fluorescence images were acquired and analyzed as previously described (section 2.6).

2.8. Circulating tumor cells/clusters (CTCs) datasets

To profile the expression of Giantin across normal and breast cancer cells in addition to circulating breast tumor cells, we used two single cell RNA-seq (scRNA-seq) datasets. The first

dataset consists of normal and breast cancer cells. Data are available in the GEO database with accession numbers GSE114727 [28]. The other dataset consists of single circulating tumor cells collected from the blood of breast cancer patients and obtained from several studies [29–36] compiled in our previous work [37]. Data are available in the GEO database with accession numbers GSE51827, GSE55807, GSE67939, GSE75367, GSE109761, GSE111065, GSE86978 and PRJNA471754. After downloading raw scRNA-seq read count data we followed a standard pre-processing pipeline to filter the cells and genes as described in our previous work [37–39]. After filtering the cells we performed the median by ratio normalization method followed by log transformation [39]. For comparison purposes among circulating tumor cells, normal and breast cancer cells, cells with Giantin expression as zero were excluded from further downstream analysis.

2.9. Computational model of tumor progression

To investigate the impact of speed and directional persistence of breast cancer cells on tumor growth, we use a 2D stochastic cell-based model inspired by the persistence random walk model [40]. Our newly developed model accounts for cell migration, proliferation, intravasation and death.

The model is based on 8 main assumptions: i) Cells are individual active agents that, for simplicity, live in a 2D section. ii) Cell movement is characterized by a given speed and directionality. iii) The 2D tissue section receives nourishment from functional blood vessels that are assumed to be perpendicular to the tissue section. iv) Cells in the nourished zone adjacent to a functional blood vessel are more likely to proliferate faster and move within this zone than leave it. v) Cell division depends on several factors, including proximity to blood vessels, local cell density and the time since the division of the corresponding mother cell. vi) Cells that spend the duration of a G1 phase in the nourished zones can have a shorter cell cycle length. vii) Cells become necrotic and die if they are not able to divide due to lack of space after several cell cycles. We also consider cells that spend prolonged periods of time without dividing, but are able to re-enter the cell cycle. We refer to those cells as "quiescent". In an in vivo situation, such cells could be quiescent, dormant or senescent. viii) Cells moving towards a blood vessel can intravasate when they get in contact with it.

The aforementioned assumptions were translated into a stochastic mathematical and computational model that is fully described and parameterized in the Table A in S1 Text. The model uses 2D continuous space and discrete time steps. Cells are described as circular agents of a given diameter and their position is determined by the coordinates of the center of the circle in a 2D computational domain. At any given time point, two cells cannot overlap, but to move from one location to another in each time step, cells can cross through locations that are occupied by other cells. Cell movement is simulated according to speed profiles computed following an empirical distribution. The directionality of a cell is determined in terms of persistence ratios, which range between 0 and 1. A persistence ratio of 1 refers to a very persistent cell, which maintained a preferred overall direction of movements within bilateral 90 degrees. Cell division is a stochastic event. The probability of a cell to divide is determined based on a proliferation score $PS = T + D + V$, that depends on three additive factors: the time since the division of the original agent (T), the local cell density (D), and proximity to blood vessels (V). At each time point, these three factors are monitored for every cell in the simulated field. The local cell density (D) is a discrete index reflecting the number of occupied spots around the target simulated cell in the Moore neighborhood (Fig G in S1 Text). The higher the number (n) of occupied spots in the Moore neighborhood, the smaller is D. However, if the Moore neighborhood of a cell is fully occupied by other cells ($n = 8$) we assume proliferation is completely

inhibited. The proximity to a blood vessel (V) describes a proliferation advantage a cell can get when it is located in well-nourished zones around blood vessels. We assumed that the proliferation rate is 30% higher in well-nourished zones. This assumption was estimated empirically and is based on literature [41–43]. The proliferation probability is high when PS is equal or higher than a predetermined cell cycle length. Instead, we assume a very low division probability when PS is lower than the cell cycle length. Additionally, we assume that after cell division, the two cells start the first phase of the cell cycle known as G1 phase. If a cell spends the needed time to complete the G1 phase (t_{G1}) in a well-nourished zone, the probability for division is switched to high, regardless of the value of PS. Based on the lifespan length of a cell, it can be classified as undergoing proliferation, quiescent or necrotic. If a cell is not undergoing cell division within a particular period of cell-cycles (n_n) then it is considered necrotic and removed from the field. Cells that did not divide within a given period of cell-cycles (n_s with $n_s < n_n$) are considered as quiescent cells. Otherwise, cells are considered to undergo proliferation. Finally, cells are removed from the field to simulate i) cell death if a cell is not undergoing cell division after a number of cell-cycles because of lack of available space. ii) intravasation if a cell succeeded in penetrating into the lumen with a given probability.

In our model, the ability of a cell to move, divide, intravasate and leave a well-nourished zone is a stochastic event. Such stochasticity is achieved by generating a uniform random number between 0 and 1 per cell per process per iteration. A process is triggered when the random number is equal to or less than the corresponding parameter value, representing the probability of the event to take place. The algorithm used for each discrete time step and for each cell is described in detail in the S1 Text. Periodic boundary conditions were imposed to simplify the implementation and to increase the computational efficiency. While the choice of periodic boundary conditions avoids losing cells out of the simulation field, it may affect the spatial distribution of cells when the tumor is large enough to get in touch with the boundaries.

In each simulation, which is characterized by certain speed and directional persistence, we accounted for the following outcomes: the number and distribution of cells in the 2D domain, the number of intravasating cells, the proliferation outcome and the mean time spent in the nourished zones. In this way we were able to estimate the optimal speed-persistence combination that leads to bigger tumors and more intravasation. We also used the model to study the pathological relevance of Golgi fragmentation in breast cancer. Computer simulations were performed mainly in HPC solutions provided by the Oslo Centre for Epidemiology and Biostatistics, at the University of Oslo and also on the Abel computer cluster, owned by the University of Oslo, and operated by the Department for Research Computing at USIT, the University of Oslo IT-department. The source code to simulate the model in addition to the simulation data are available at https://github.com/ocbe-uio/Cancer_simulator.

3. Results

3.1. The effect of cell speed and persistence on tumor progression

Two of the most intuitive parameters to characterize cell movement are the speed and directional persistence. We first investigated the impact of these two parameters on tumor growth and intravasation using computational modeling. Our model accounted for cell migration, proliferation, intravasation, and cell death (see the Methods section and Table A in S1 Text for a full description of the model and its parameterization). Briefly, cells were freely moving in a two-dimensional space, were assigned a certain rate of division, and were assumed to die if they had not performed a division for longer than three doubling times. This allowed us to simulate cell death and thereby tumor necrosis in poorly nourished areas. To account for growth advantage and attraction of the well-nourished areas close to blood vessels, cells were

assigned a lower likelihood to leave this area and were given a 30% growth advantage (faster doubling). We implemented extensive numerical simulations of 130 speed-persistence combinations. We used live epifluorescence imaging of cells (BT549 and MDA-MB-231) migrating freely in 2D followed by automated tracking to infer a realistic range of parameter space for persistence and speed (see Figs I and J in S1 Text for the experimental outcome). For each simulation of a 90 days period, we computed the changes in the number and distribution of cancer cells. We characterized the spatial cell distribution using the uniformity index (*UI*) [44–46]. High *UI* indicates a homogeneous distribution all over the simulation field, whereas low *UI* is an indication for cluster formation. Due to the model stochasticity, simulations were repeated twenty five times for each speed-persistence combination (see S1 Video).

Simulations showed that cell speed and persistence have a profound effect on the distribution of cancer cells generating tumors with different uniformity indices (*UIs*) (Fig 1A). At very low speed, the simulation produced tumors that were very compact and in the extreme case exhibited signs of tumor necrosis in the center of very compact tumors (see insets in Figs 1A and A in S1 Text, panels A and B). A key prediction of our in silico simulations is that the size of the tumor increases with both speed and persistence of cell migration (Fig A in S1 Text, panel C). The impact of speed was stronger than that of persistence. When a fixed persistence value was used, increasing the speed had a major impact on the number of cells in the tumor (Fig 1B). The impact of persistence on the size of the tumor was barely noticeable at low speeds (Fig A in S1 Text, panel D).

Cells moving towards and contacting a blood vessel were assigned a certain probability of leaving the tumor by intravasation. We assigned a probability of 1:10000 (0.01%) of a cancer cell to leave the primary tumor. This number is a pure estimate based on the assumption that a tumor with a mass of 1 gram would contain around 10^8 cells [47] and the number of circulating tumor cells is between 1–3 CTCs per ml of blood assuming an average human to have 5L of blood. Simulations showed that the number of intravasating cells increased with speed only (Fig A in S1 Text, panel E). Under the same persistence condition, speed had a strong impact on the number of intravasating cells, but no effect on persistence was observed when the speed was kept constant (Fig 1C and 1D). This is most likely because speed has a stronger impact on the total number of cells in the tumor and it is intuitive to assume that larger tumors will produce more intravasating cells.

3.2. Golgi fragmentation in breast cancer tissue

Next, we sought to explore the biological significance of our computational model. As stated above, alterations of Golgi structure are well known to affect cell migration [6,15]. Thus, we decided to test the pathophysiological relevance of our model predictions by investigating cell migration traits associated with a condition that induces Golgi fragmentation. Although the role of the Golgi in tumor progression has been discussed in the literature [6,13,48,49], there is surprisingly little experimental evidence for structural alterations of the Golgi in patient-derived tumor tissue. Golgi fragmentation has been reported in colorectal cancer [50] and prostate cancer [51], but to the best of our knowledge no analysis of a Golgi structure in breast cancer tissue is available. Thus, before directly investigating a specific condition that induces Golgi fragmentation, we wanted to assess Golgi structure in patient-derived xenograft (PDX) samples from triple-negative basal-like, or hormone receptors positive luminal B tumor tissue (Fig 2A and 2B). In the triple-negative tumors, Golgi fragmentation was observed in 50% of the examined cells whereas only 41% of the hormone receptors positive tumors contained fragmented Golgi. The prevalence of this phenotype tempts to speculate about a relevance of Golgi fragmentation in breast cancer pathology. This notion is further supported by the observation

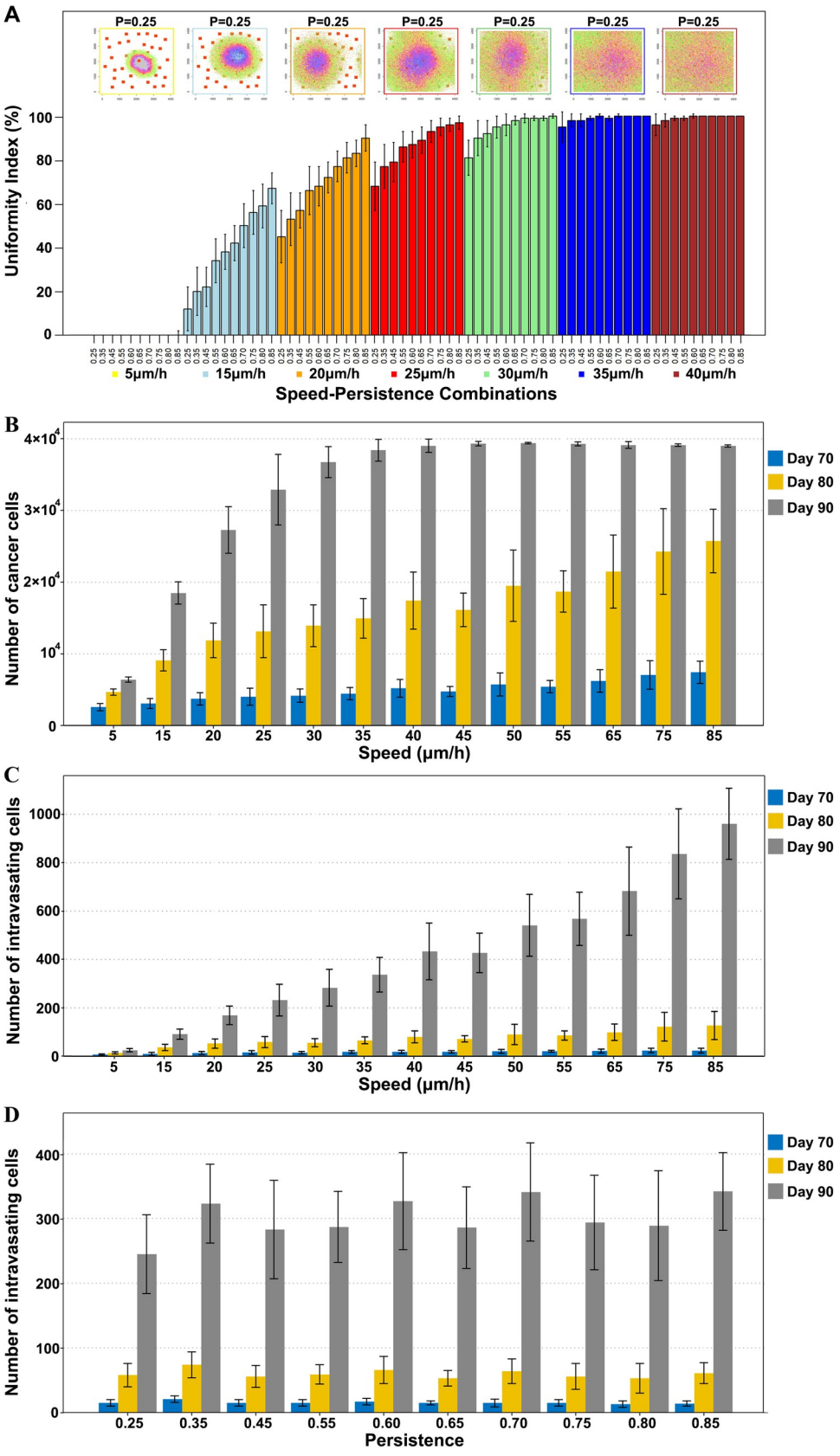
A
P=0.25
P=0.25
P=0.25
P=0.25
P=0.25
P=0.25
P=0.25
Uniformity Index (%)
5μm/h
15μm/h
20μm/h
25μm/h
30μm/h
35μm/h
40μm/h
Speed-Persistence Combinations
B
Number of cancer cells
Day 70
Day 80
Day 90
Speed (μm/h)
C
Number of intravasating cells
Day 70
Day 80
Day 90
Speed (μm/h)
D
Number of intravasating cells
Day 70
Day 80
Day 90
Persistence

Fig 1. Effect of cell speed and persistence on tumor growth and intravasation. (A) Upper plots illustrate how the distribution of cancer cells at the end of the simulation changes for different speeds and the same fixed persistence (P = 0.25). Each of these plots is a representative simulation field of a 2D tumor section characterized with a particular speed. Cell colors represent the time cells are generated. While green-pink labels represent cells that have divided more recently, purple-blue cells have divided a longer time ago. Necrotic areas are labeled with a gray mask. Bars represent the mean uniformity index of twenty five simulation replicates. Different colors refer to different speeds. Within one color, persistence gradually increases. (B) Number of cancer cells at different time points across gradual speed but fixed persistence (P = 0.45). (C) Number of intravasating cells at different time points across gradual speed but fixed persistence (P = 0.45). (D) Number of intravasating cells at different time points across gradual persistence value but fixed speed of 30um/h. Error bars represent the standard deviation of the data.

https://doi.org/10.1371/journal.pcbi.1010995.g001

of the higher prevalence of Golgi fragmentation in samples from invasive ductal carcinoma compared to adjacent normal breast tissue (Fig B in S1 Text, panels A and B).

3.3. Giantin is a Golgi protein that might be involved in breast cancer progression

Previous work has identified several genes whose depletion may result in Golgi fragmentation [14,16]. However, because these data are from siRNA screens, it remains largely unclear whether these gene depletions induce Golgi fragmentation in a direct manner. Thus, we decided to focus on Golgi matrix proteins and tested whether their levels are linked to survival of breast cancer patients using the kmplot database [52,53]. We focused on six matrix proteins that have a relatively well understood role in maintaining Golgi morphology (*GOLGA1*, *GOLGA2*, *GOLGA3*, *GRASP55*, *GOLGB1* and *GORASP1*). With the exception of *GRASP55* and *GOLGA3*, there was a significant trend indicating that low expression correlates with poor survival (Fig C in S1 Text). This trend was very strong for Giantin (also known as *GOLGB1*, Fig 2C) and therefore we decided to focus on this Golgi matrix protein for further studies. Silencing Giantin expression in BT549 cells and MDA-MB231 cells worked reproducibly and induced a fragmentation of the Golgi (Figs 2D and 2F and D in S1 Text, panel A). To investigate the migratory pattern of BT549 cells upon Giantin knockdown, we analyzed the trajectories of cells that were freely migrating on a 2D surface. Cells were scaled and projected based on their root mean square speed and persistence ratio. Scaling was done by normalizing them to the mean values, which were assigned a value of 1. Using this approach, we defined four groups with distinct migration and persistence values: group 1 (low speed, low persistence), group 2 (low speed, high persistence). group 3 (high speed, low persistence) and group 4 (high speed, high persistence) (Fig 3A). In comparison to control cells, BT549 cells lacking Giantin were preferentially found in the low-speed groups 1&2 (Figs 3B–3D and D in S1 Text, panel B). On the other hand, cell persistence was not appreciably affected by the depletion of Giantin (Fig D in S1 Text, panels C and D). Seeing these experimental results through the lens of our computational model, the migration pattern of Giantin depleted cells would result in a smaller tumor, which we expect to seed fewer intravasating cells. This is difficult to reconcile with the fact that patients with lower Giantin exhibit lower disease-free survival rates (Fig 2C). Our simulations were all carried out with a fixed rate of intravasation and therefore, it appears intuitive that smaller tumors would produce less intravasating cells. Thus, we asked to what extent must the rate of intravasation of a smaller tumor increase to produce more intravasating cells than a bigger tumor? We therefore re-run our simulations with adjustments of the rates of intravasation. To better link these new simulations to our experimental data, we took into account the number of cells with Golgi fragmentation in conditions of Giantin knockdown, where we observed that 65% of cells display a fragmented Golgi. We assumed that the cells with fragmented Golgi are the ones with the highest level of Giantin knockdown where the biological effects (*i.e.* slower cell migration) is also expected to be strongest. In the simulations, tumors

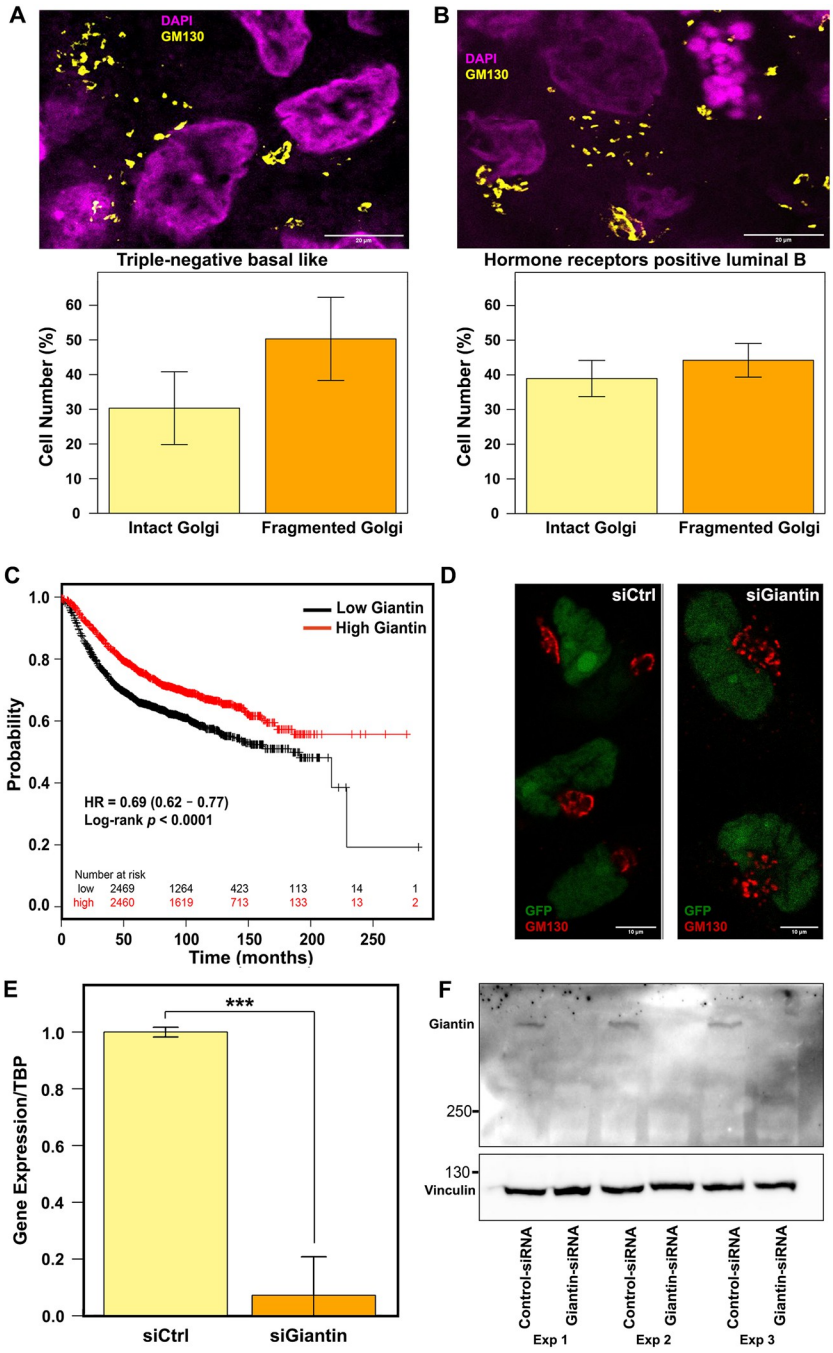

Fig 2. Immunofluorescence staining for Golgi marker Giantin. (A) Representative images of triple-negative basal like PDX samples (upper panel). Bar plot showing the percentage of cells with intact and fragmented Golgi (lower panel) in different triple-negative basal like PDX samples (MAS98.12 and HBCx-39; n = 4 with 25 fields each). (B) Representative images of hormone receptors positive luminal B PDX samples (upper panel). Bar plot showing the percentage of cells with intact and fragmented Golgi (lower panel) in different hormone receptors positive luminal B PDX samples (MAS98.06 and HBCx-34; n = 4 with 25 fields each). Error bars represent standard deviation of the data. (C) Kaplan–Meier survival curves in patients with high and low Giantin expression. The graph was generated using the kmplot database (https://kmplot.com/) (D) Representative image of BT549 cells stably expressing nuclear GFP were transfected with Ctrl or Giantin siRNA. After 72 h, cells were fixed and immunostained against GM130 to label the Golgi (red). (E) Barplot showing the average values of the relative gene expression (ΔΔCq method by qPCR) of Giantin from 3 biological replicates in BT549 cells. Cells were harvested 72 h after siRNA transfection. Statistical significance was determined using Kruskal-Wallis rank sum test (*** $p < 0.001$). (F) Immunoblot from 3 independent experiments in MDA-MB-231 cells harvested 72 h after transfection with control or Giantin siRNA. Cells were lysed and immunoblotted against Giantin (upper blot) and against vinculin (lower blot) to probe for equal loading.

https://doi.org/10.1371/journal.pcbi.1010995.g002

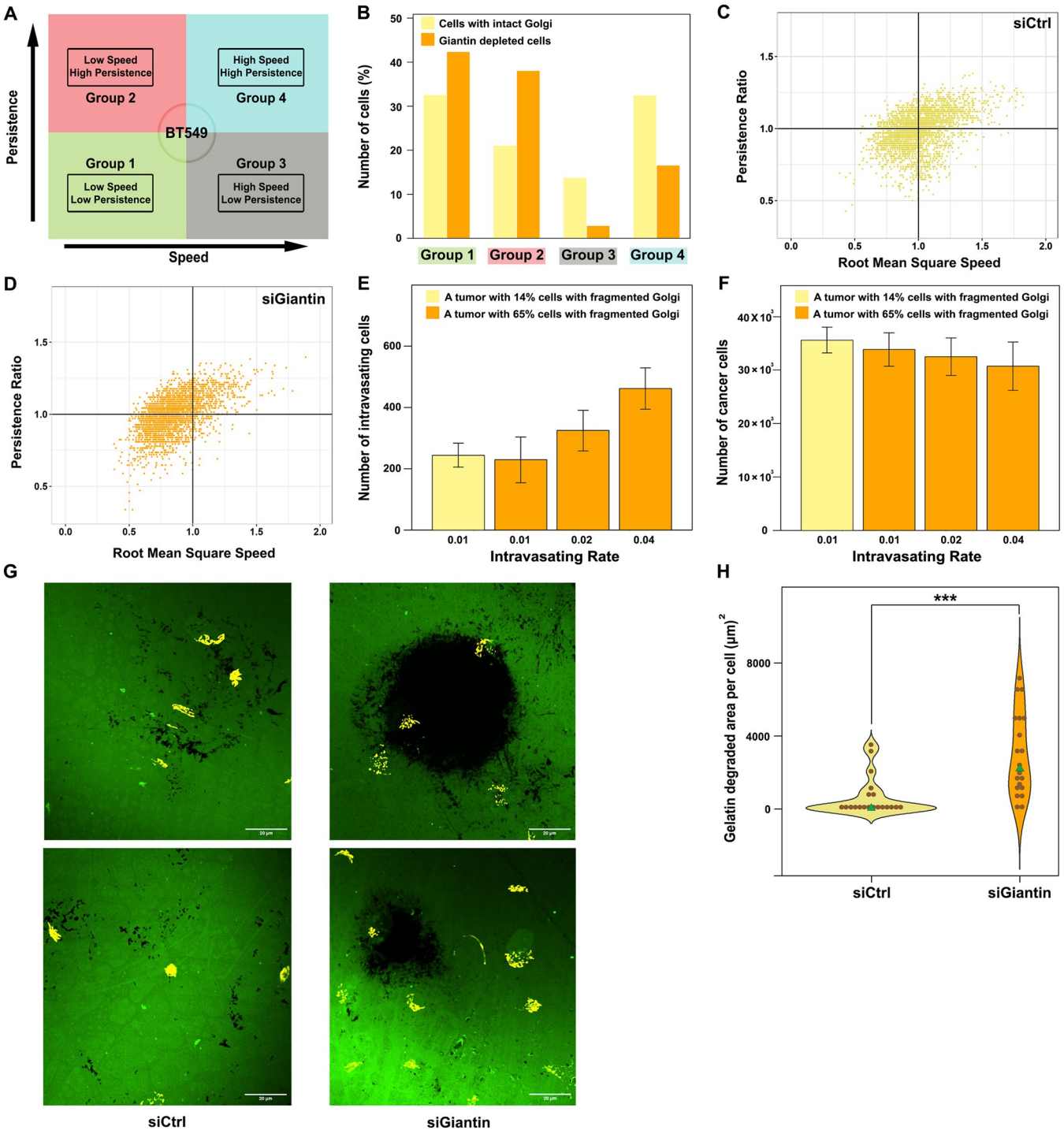

Fig 3. BT549 migration and invasion. (A) A schema showing the four groups of BT549 cells based on speed and persistence. (B) Bar plot showing the distribution of cells in each group. (C) The four migratory fashion groups of 2850 BT549 control cells pooled from 3 experiments. (D) The four migratory fashion groups of 2800 BT549 cells with Giantin knockdown pooled from 3 experiments. (E-F) Simulated impact of increasing the intravasating rate of cells with fragmented Golgi on the total number of intravasating cells and total number of simulated cells. Error bars represent the standard deviation of twenty five replicates. (G) Representative confocal immunofluorescence images of fluorescent gelatin degradation assay in BT549 cells. Degraded areas are visualized in black. The Golgi is visualized in yellow. (H) Violin plot showing the quantification of the gelatin-degraded area. Green triangles represent the median value. Black dots represent the gelatin-degraded area normalized to cell number. Statistical significance is assessed by Kruskal-Wallis rank sum test (*** $p < 0.001$), n = 20 microscopic fields from 2 independent experiments.

https://doi.org/10.1371/journal.pcbi.1010995.g003

with low Giantin, were considered to have 65% of cells with slower cell migration. Because control conditions exhibited 14% of cells with Golgi fragmentation, we used this value for the simulation of tumors with high levels of Giantin. The higher the number of cells with Golgi fragmentation, the smaller the tumor and the less intravasated cells it produced. This is to be expected, because Golgi fragmentation (induced by Giantin depletion) slows cells migration, which in our model reduces the size of the tumor, thereby having less cells than can intravasate. When we assigned the Giantin-depleted tumor a 2-fold higher intravasation rate, we observed that it produced a similar amount of intravasated cells compared to control conditions with only 14% fragmented Golgi (Fig 3E). Of note, the tumor with 65% Golgi fragmentation was still smaller (Fig 3F) indicating that the increase in intravasation rate can overcome the effect of the size of the primary tumor. Increasing the intravasation rate by 4-fold allowed the tumors with high degree of Golgi fragmentation to seed more intravasated cells (Fig 3E), which again could not be explained by the tumor size (Fig 3F). Based on this, we hypothesized that increasing the invasion rate by at least 4-fold would allow smaller tumors to seed more circulating tumors cells, which might give rise to more metastasis and hence explain poor patient survival.

To experimentally test whether Giantin depleted cells exhibited higher invasion rates, we tested their ability to degrade extracellular matrix. To this end, cells were seeded on glass cover slips coated with fluorescent gelatin. By analyzing the pattern and size and the area of the digested gelatin we found that silencing Giantin resulted in a marked increase of the median ability of cells to degrade gelatin. This increase ranged from a few percent to more than 30-fold (see violin plot and representative images in Fig 3G and 3H).

To predict the pathological relevance of Giantin loss in breast cancer we expanded our *in silico* model to account for a higher rate of invasion which we observed experimentally. The revised model had three additional assumptions: 1) each cell in the tumor has a probability of developing the low Giantin phenotype; 2) cells with low Giantin have higher invasiveness, which yields to higher intravasating capability; 3) cells follow the migratory phenotype of one of the four aforementioned groups based on the percent abundance of the groups. The *in silico* outcome of tumor progression in two independent populations (S2 Video) that diverge in the percent abundance of cells with low Giantin (14% and 65%) shows significant difference in terms of uniformity index, number of generated cells and number of intravasating cells (Fig 4A). Furthermore, we tested the impact of increasing fraction of low-Giantin cells in the population (0%, 25%, 50%, 75% and 100%) on tumor progression (S3 Video). The results show that the higher the fraction of cells with low Giantin, the lower the uniformity index and the smaller the tumor but with higher intravasation capability (Fig 4B and 4D). The number of intravasating cells in a population of a thousand cancer cells was found to be statistically significant among all the different groups with the highest number (30 ± 4) in a pure population of cells with low Giantin expression (Fig E in S1 Text). Thus, the combination of our mathematical and cell biological experiments provides a possible explanation for the poor disease-free survival of patients with low Giantin levels.

3.4. *Giantin* expression in breast cancer patients

Because our simulation results suggest that loss of Giantin increases the invasive capability of tumor cells to intravasate into the circulation, we would expect circulating tumor cells to have lower Giantin expression than the primary tumor. To test this hypothesis, first we investigated the expression of Giantin in circulating breast tumor cells ($n = 1448$) compared to a housekeeping gene (*ACTB*) (Fig 5A). Then, we profiled the expression of Giantin in individual cancer cells (n = 168) and adjacent normal breast cells ($n = 1500$) collected from patients with

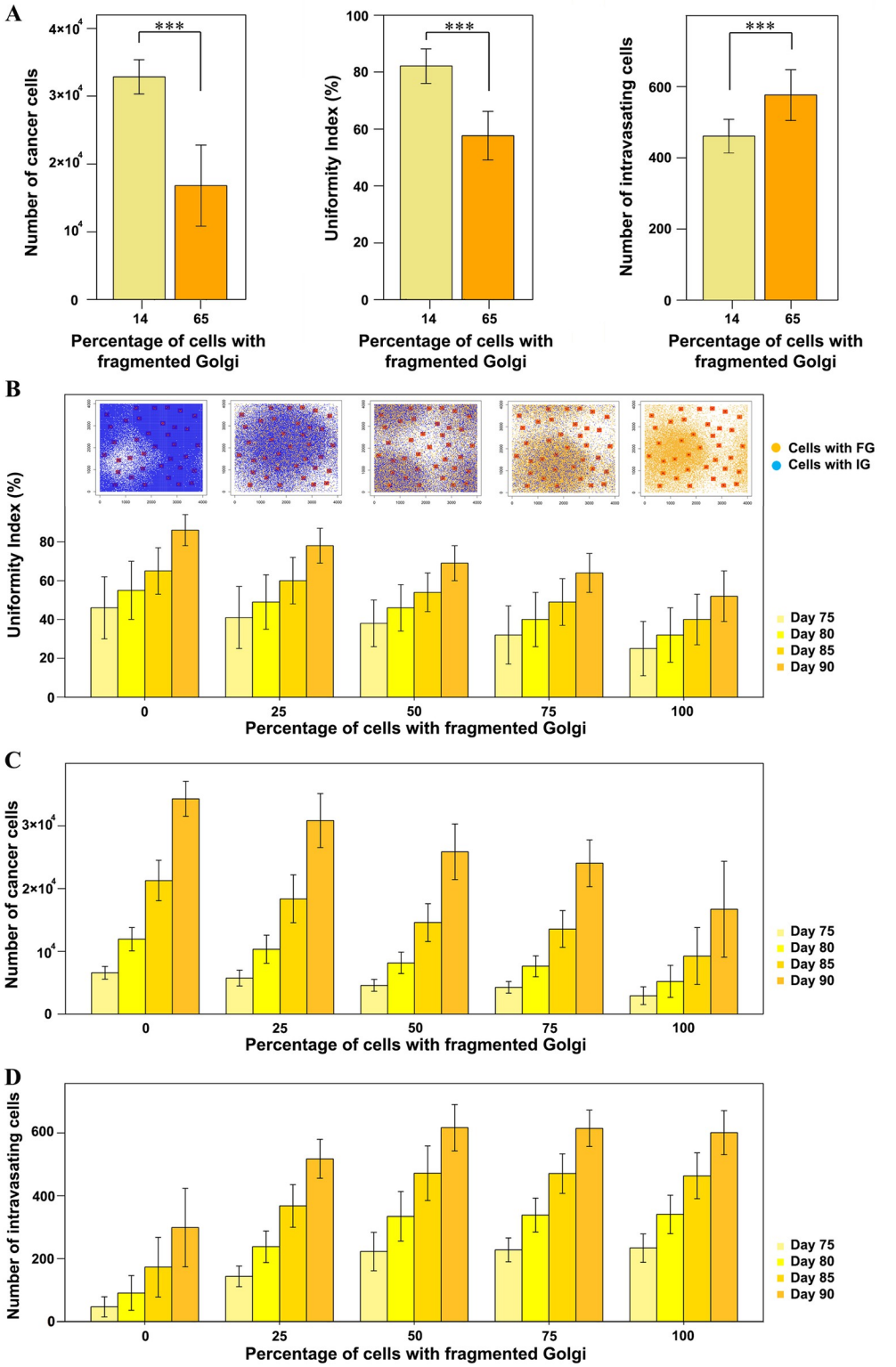

Fig 4. Impact of loss of Giantin on tumor growth and intravasation. (A) Modeling outcome of a tumor with 14% cells with fragmented Golgi versus a tumor with 65% cells with fragmented Golgi. Statistical significance was determined using two sample t-test (*** $p < 0.001$), (B) Upper plots demonstrate the distribution of cancer cells after 90 days from the tumor initiation with different percent abundance values of cells with fragmented Golgi. Cells with an intact Golgi (IG) are depicted in blue and cell with a fragmented Golgi (FG) are depicted in yellow. Bars represent

mean uniformity index of twenty five replicates. Different colors refer to different time points. (C) Number of cancer cells at different time points across gradual percent abundance values of cells with fragmented Golgi. (D) Number of intravasating cells at different time points across gradual percent abundance values of cells with fragmented Golgi. Error bars represent the standard deviation of twenty five replicates.

https://doi.org/10.1371/journal.pcbi.1010995.g004

breast cancer in addition to circulating breast tumor cells (n = 627). The single-cell RNA-seq analysis showed significant gradual decrement in mRNA levels of Giantin across the three datasets with lowest expression in the circulating breast tumor cells (0.24 ± 0.81) compared to primary breast cancer cells (0.99 ± 0.96) and their adjacent normal breast cells (1.84 ± 0.76) (Fig 5B). On the other hand, we observed a marginal difference in the expression of a house-keeping gene (*ACTB*) (Fig 5C).

4. Discussion

In addition to state-of-the art experiments, mathematical and computational models provide insights into complex cancer processes including tumor growth [54,55], metastasis [56–58], treatment response [56,59–64] and cell migration and invasion in 2D and 3D matrices [65–68]. In particular, cell-based models have been recently applied to investigate the roles of proliferation, migration, and necrosis in tumor progression of different cancers (reviewed in [69]). The present study represents a new step in understanding the impact of different traits of cell migration on the progression of breast cancer through an integrated experimental-computational approach. Thereby, we provide a possible explanation for the poor survival of breast cancer patients with low expression of Giantin. Loss of this Golgi matrix protein results in fragmentation of the Golgi apparatus, a phenomenon that we found to be very prevalent in patient-derived breast cancer specimens. Our computational approach shows that a simple model accounting for cellular activities and migratory characteristics can be used to study tumor size and the intravasation rate over a given time. Importantly, our model suggests that cells with lower speed lead to a smaller and more compact tumor. Because silencing Giantin led to a reduction in migration speed, our model predicts that tumors with low Giantin expression would be smaller in size. Thus, our computational model indicated the need for further experimental results to explain the clinical survival data. We then noted that silencing Giantin enhanced invasiveness of breast cancer cells and through further computational simulations, we found that this enhanced invasiveness could overcome the effect of the smaller size such

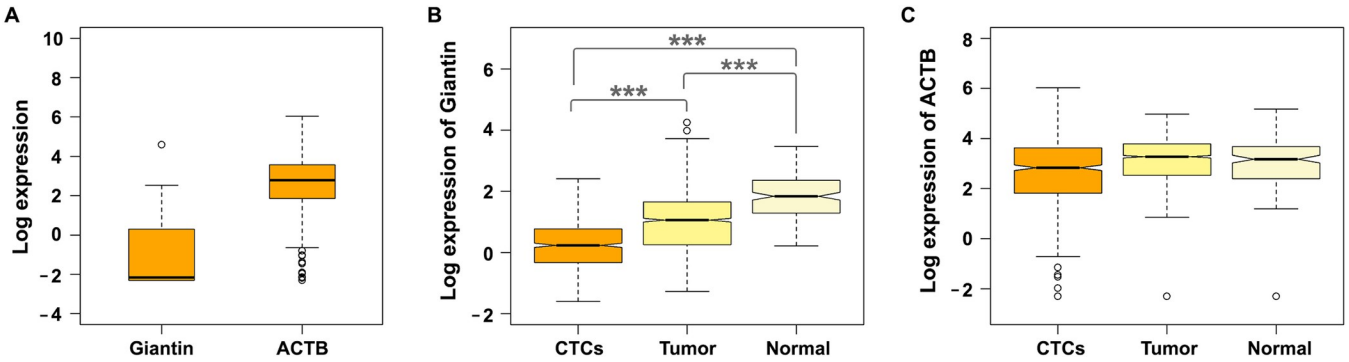

Fig 5. Giantin expression profile. (A) Boxplot showing the expression of Giantin and actin (ACTB) at single cell level in CTCs (n = 1448). (B) Boxplot showing the expression of Giantin at single cell level in CTCs (n = 627), breast tumor (n = 168) and adjacent normal breast (n = 1500). Statistical significance was determined using the Kruskal–Wallis rank sum test, followed by pairwise comparisons using the Wilcoxon rank sum test (*** $p < 0.001$). (C) Boxplot showing the expression of actin (ACTB) at single cell level in CTCs (n = 627), breast tumor (n = 168) and adjacent normal breast (n = 1500).

https://doi.org/10.1371/journal.pcbi.1010995.g005

that Giantin-low tumors would produce more circulating tumor cells. This notion is the observation that CTCs express lower Giantin levels than the primary tumor.

Several questions arise from our work. One question is whether the compactness of tumors with lower Giantin levels can be validated clinically. Based on this, it will be interesting to evaluate the chemosensitivity of tumors with different levels of compactness. It is possible that chemotherapeutics might have less access to compact tumors, thus making these tumors more likely to relapse after an initial round of therapy. Our mathematical model focused mainly on the cancer cells and did not consider the role of cancer associated fibroblasts or the tumor stroma. It is possible that Giantin-low tumors might be smaller, but also less compact due to the higher invasiveness. Indeed, less compact tumors were found to be associated with lymphovascular space invasion and the formation of lymph node metastases [70]. Our model and the experimental follow-up do not allow to determine how the Giantin-low trait is being selected for. While the acquisition of a more invasive phenotype is an advantage for intravasation, it appears counterintuitive to select for a trait that would cause a growth disadvantage. However, it is possible that this switch between a pro-invasive trait and a pro-growth trait is a reflection of this phenotypic plasticity that is well known in tumors. It is also possible that the invasive phenotype might alter the interaction of cancer cells with their microenvironment and thereby alter tumorigenesis in a way that can only be investigated using in vivo imaging techniques and is therefore beyond the scope of the current study.

The exact explanation of the elevated invasion capability of cells with low Giantin is not yet clear but a few possible scenarios can be hypothesized. One possible explanation is that Giantin depleted cells exhibit a reduction in their speed, thus having more time for efficient degradation of the collagen while moving slowly on top of it. Another scenario is that silencing Giantin induces the expression of matrix metalloproteinases (MMPs) to degrade many components of the extracellular matrix. Finally, there is evidence that fragmentation of the Golgi enhances the rate of intra-Golgi trafficking [71]. Although this has so far only been shown in the context of neurodegeneration, it is possible that a fragmented Golgi would accelerate the secretory transport of MMPs and thereby enhance extracellular matrix degradation.

Taken together, our work used a combination of mathematical modeling and wet-lab experiments and proposed that the speed of cancer cell migration has a major impact on the shape and size of a tumor and this may explain how loss of Giantin could contribute to the process of tumorigenesis.

Supporting information

S1 Text. ***Fig A. Impact of cell speed and persistence on tumor progression.*** *(A) Strong negative correlation between number of necrotic cells and uniformity index (Pearson correlation coefficient = -0.76). (B) Weak negative correlation between number of* quiescent *cells and uniformity index (Pearson correlation coefficient = -0.24). (C) Number of cancer cells after 90 days from the tumor initiation across different speed-persistence combinations. (D) Number of cancer cells at different time points (blue*: *day 70, yellow*: *day 80 and gray*: *day 90) across gradual persistence value but fixed speed of 30um/h. (E) Number of intravasating cells after 90 days from the tumor initiation across different speed-persistence combinations.* Error bars represent *the* standard deviation *of twenty five replicates.* ***Fig B. Immunofluorescence staining for Golgi marker giantin (yellow).*** *(A) Representative image of adjacent normal breast tissue patient samples. (B) Representative image of invasive ductal carcinoma patient section.* ***Fig C. Kaplan–Meier survival curves*** *for* six matrix proteins that have a relatively well understood role in maintaining Golgi morphology (*GOLGA1*, *GOLGA2*, *GOLGA3*, *GRASP55*, *GOLGB1* and *GORASP1*). ***Fig D. Impact of Golgi fragmentation on cell migration.*** *(A) Percentage of cells denoted with*

fragmented Golgi in BT549 cells. (B) Bar plot showing the percentage of cells based on speed, low speed includes group 1&2 whereas high speed includes group 3&4. (C) Bar plot showing the percentage of cells based on persistence, low persistence includes group 1&3 whereas high persistence includes group 2&4. (D) Bar plot showing the averaged persistence ratio per group. ***Fig E. Number of intravasating cells in a population of a thousand cancer cells.*** *Statistical significance was determined using the Kruskal–Wallis rank sum test, followed by pairwise comparisons using the Wilcoxon rank sum test with Bonferroni* Correction (* $p < 0.05$, *** $p < 0.001$). ***Fig F. Cell's speed-persistence.*** *(A) 5-day speed profile. (B) Schematic chart explaining how the persistence ratio is computed for a cell that moved from a to b.* ***Fig G. Simulation field and the local density.*** *(A) A 2D section showing the architecture of the simulated tumor field. Black squares represent the lumen of blood vessels. Red squares represent the well-nourished zones. The blue circle represents a single cancer cell. (B) Schema explaining the way of computing the local cell density.* ***Fig H. Simulating the position of the new movement of the second daughter cell resulted from division of the original cell.*** *(A) Location of the original cell before (magenta) and after (black) division, the black line represents the distance between the initial location of the second cell and the new location. (B) All possible locations of the new location of the second cell. (C) Possible locations in case of forward movement (red dots) or backward movement (orange dots). (D) Excluding the spots occupied by other cells. (E) Stochastic selection of the location of the the new location of the second cell in case of forward movement (red dot) or backward movement (orange dot).* ***Fig I. Experimental observations of BT548 and MDA-MB-231 cells.*** *(A) Violin plot showing of reported mean diameter of MDA-MB-231 in the several studies and in-house microscopic observation. Median cell diameter is shown in red whereas the mean is shown in orange. (B) line plot showing the number of BT549 cells* cultured in RPMI medium containing 3%, 9% or 15% serum *at three different time points. (C) Quantification of the gelatin-degraded area. Bars represent the median value. Error bars represent quantile-based coefficient of variation relative to control cells by Kruskal-Wallis chi-squared test (*** $p < 0.001$), $n = 13$ microscopic fields from 2 independent experiments.* ***Fig J. Experimental observations of Bt548 and MDA-MB-231 cells.*** *(A) Violin plot showing the distribution of the values of root mean square speed for BT549 and MDA_MB_231 cells. (B) Violin plot showing the distribution of the values of persistence ratio for BT549 and MDA_MB_231 cells. (C) Cartesian product of the persistence ratio and the root mean square speeds used for the modeling. (D) A scatterplot showing the relationship between the persistence ratio and the root mean square speeds of BT549 cells (orange) and MDA_MB_231 cells (gray). (E) Movement options of simulated cells. Black arrow represents the previous movement. Red triangles represent the possible locations of a forward movement whereas orange triangles represent the possible locations of a backward movement.* ***Fig K. Simulating cell movements.*** *(A) A schema with a panel of mathematical equations explaining how the X and Y coordinates of the new movement are computed. (B) Possible locations in case of forward movement (red dots) or backward movement (orange points). (C) A stochastic selection of a forward movement from P2 to P3 and a backward movement from P2 to P4.* ***Fig. The simulation field.*** (A) *Moore neighborhood. (B) Moore neighborhood in periodic boundary conditions. (C) The grid-based spatial reference system embedded on top of the 2D simulation field, arrows show the increase in the lattice square numbering.* ***Table A***. A description of the parameters used in the proposed model. ***Table B***. Parameters used in the proposed model with their corresponding computational name.
(DOCX)

S1 Video. Six simulation examples showing different speed-persistence combinations.
(MP4)

S2 Video. Two simulation examples showing the in-silico outcome of tumor progression in two independent populations that diverge in the percent abundance of cells with low Giantin (14% and 65%).
(MP4)

S3 Video. Five simulation examples showing the in-silico outcome of tumor progression in different independent populations that diverge in the percent abundance of cells with low Giantin.
(MP4)

Acknowledgments

Computer simulations were performed mainly in HPC solutions provided by the Oslo Centre for Epidemiology and Biostatistics, at the University of Oslo and also on the Abel computer cluster, owned by the University of Oslo, and operated by the Department for Research Computing at USIT, the University of Oslo IT-department. http://www.hpc.uio.no/

Author Contributions

Conceptualization: Salim Ghannoum, Veronika Reiterer, Alvaro Köhn-Luque, Hesso Farhan.

Data curation: Salim Ghannoum, Arvind Iyer, Debarka Sengupta.

Formal analysis: Salim Ghannoum.

Investigation: Salim Ghannoum, Hesso Farhan.

Methodology: Muhammad Zahoor, Veronika Reiterer, Santosh Phuyal, Lina Prasmickaite, Gunhild Mari Mælandsmo.

Software: Salim Ghannoum, Damiano Fantini, Waldir Leoncio Netto, Øystein Sørensen.

Supervision: Alvaro Köhn-Luque, Hesso Farhan.

Validation: Salim Ghannoum.

Visualization: Salim Ghannoum.

Writing – original draft: Salim Ghannoum, Alvaro Köhn-Luque, Hesso Farhan.

Writing – review & editing: Salim Ghannoum, Damiano Fantini, Muhammad Zahoor, Veronika Reiterer, Waldir Leoncio Netto, Arvind Iyer, Debarka Sengupta, Lina Prasmickaite, Gunhild Mari Mælandsmo, Alvaro Köhn-Luque, Hesso Farhan.

References

1. Bray F, Ferlay J, Soerjomataram I, Siegel RL, Torre LA, Jemal A. Global cancer statistics 2018: GLOBOCAN estimates of incidence and mortality worldwide for 36 cancers in 185 countries. CA: a cancer journal for clinicians. 2018; 68(6):394–424. https://doi.org/10.3322/caac.21492 PMID: 30207593
2. Kabel AM, Baali FH. Breast cancer: insights into risk factors, pathogenesis, diagnosis and management. Journal of Cancer Research and Treatment. 2015; 3(2):28–33.
3. Scully OJ, Bay B-H, Yip G, Yu Y. Breast cancer metastasis. Cancer Genomics-Proteomics. 2012; 9 (5):311–20. PMID: 22990110
4. Redig AJ, McAllister SS. Breast cancer as a systemic disease: a view of metastasis. Journal of internal medicine. 2013; 274(2):113–26. https://doi.org/10.1111/joim.12084 PMID: 23844915
5. Eger A, Mikulits W. Models of epithelial–mesenchymal transition. Drug Discovery Today: Disease Models. 2005; 2(1):57–63.

6. Millarte V, Farhan H. The Golgi in cell migration: regulation by signal transduction and its implications for cancer cell metastasis. The Scientific World Journal. 2012;2012. https://doi.org/10.1100/2012/498278 PMID: 22623902
7. Bui S, Mejia I, Díaz B, Wang Y. Adaptation of the Golgi Apparatus in Cancer Cell Invasion and Metastasis. Frontiers in Cell and Developmental Biology. 2021:3582. https://doi.org/10.3389/fcell.2021.806482 PMID: 34957124
8. Yadav S, Puri S, Linstedt AD. A primary role for Golgi positioning in directed secretion, cell polarity, and wound healing. Molecular biology of the cell. 2009; 20(6):1728–36. https://doi.org/10.1091/mbc.e08-10-1077 PMID: 19158377
9. Ladinsky MS, Mastronarde DN, McIntosh JR, Howell KE, Staehelin LA. Golgi structure in three dimensions: functional insights from the normal rat kidney cell. The Journal of cell biology. 1999; 144 (6):1135–49. https://doi.org/10.1083/jcb.144.6.1135 PMID: 10087259
10. Koreishi M, Gniadek TJ, Yu S, Masuda J, Honjo Y, Satoh A. The golgin tether giantin regulates the secretory pathway by controlling stack organization within Golgi apparatus. PloS one. 2013; 8(3): e59821. https://doi.org/10.1371/journal.pone.0059821 PMID: 23555793
11. Satoh A, Hayashi-Nishino M, Shakuno T, Masuda J, Koreishi M, Murakami R, et al. The golgin protein giantin regulates interconnections between golgi stacks. Frontiers in cell and developmental biology. 2019; 7:160. https://doi.org/10.3389/fcell.2019.00160 PMID: 31544102
12. Stevenson NL, Bergen DJ, Lu Y, Prada-Sanchez ME, Kadler KE, Hammond CL, et al. Giantin is required for intracellular N-terminal processing of type I procollagen. Journal of Cell Biology. 2021; 220 (6):e202005166. https://doi.org/10.1083/jcb.202005166 PMID: 33944912
13. Petrosyan A. Onco-Golgi: is fragmentation a gate to cancer progression? Biochemistry & molecular biology journal. 2015; 1(1). https://doi.org/10.21767/2471-8084.100006 PMID: 27064441
14. Chia J, Goh G, Racine V, Ng S, Kumar P, Bard F. RNAi screening reveals a large signaling network controlling the Golgi apparatus in human cells. Mol Syst Biol. 2012; 8:629. Epub 2012/12/06. https://doi.org/10.1038/msb.2012.59 PMID: 23212246; PubMed Central PMCID: PMC3542528.
15. Millarte V, Boncompain G, Tillmann K, Perez F, Sztul E, Farhan H. Phospholipase C γ1 regulates early secretory trafficking and cell migration via interaction with p115. Molecular biology of the cell. 2015; 26 (12):2263–78.
16. Simpson JC, Joggerst B, Laketa V, Verissimo F, Cetin C, Erfle H, et al. Genome-wide RNAi screening identifies human proteins with a regulatory function in the early secretory pathway. Nature cell biology. 2012; 14(7):764–74. https://doi.org/10.1038/ncb2510 PMID: 22660414
17. Farhan H, Wendeler MW, Mitrovic S, Fava E, Silberberg Y, Sharan R, et al. MAPK signaling to the early secretory pathway revealed by kinase/phosphatase functional screening. J Cell Biol. 2010; 189(6):997–1011. Epub 2010/06/16. https://doi.org/10.1083/jcb.200912082 PMID: 20548102; PubMed Central PMCID: PMC2886346.
18. Baschieri F, Uetz-von Allmen E, Legler DF, Farhan H. Loss of GM130 in breast cancer cells and its effects on cell migration, invasion and polarity. Cell Cycle. 2015; 14(8):1139–47. https://doi.org/10.1080/15384101.2015.1007771 PMID: 25892554
19. Gallaher JA, Brown JS, Anderson AR. The impact of proliferation-migration tradeoffs on phenotypic evolution in cancer. Scientific reports. 2019; 9(1):1–10.
20. Jamous S, Comba A, Lowenstein PR, Motsch S. Self-organization in brain tumors: how cell morphology and cell density influence glioma pattern formation. PLoS computational biology. 2020; 16(5): e1007611. https://doi.org/10.1371/journal.pcbi.1007611 PMID: 32379821
21. Comba A, Faisal SM, Dunn PJ, Argento AE, Hollon TC, Al-Holou WN, et al. Spatiotemporal analysis of glioma heterogeneity reveals COL1A1 as an actionable target to disrupt tumor progression. Nature communications. 2022; 13(1):1–23.
22. Ghannoum S FD, Leoncio W, Sørensen Ø cellmigRation: Track Cells, Analyze Cell Trajectories and Compute Migration Statistics. R package version 1.2.0,. Bioconductor. 2021.
23. DuChez BJ. Automated tracking of cell migration with rapid data analysis. Current protocols in cell biology. 2018; 76(1):12. 1-.. 6.
24. Bergamaschi A, Hjortland GO, Triulzi T, Sørlie T, Johnsen H, Ree AH, et al. Molecular profiling and characterization of luminal-like and basal-like in vivo breast cancer xenograft models. Molecular oncology. 2009; 3(5–6):469–82. https://doi.org/10.1016/j.molonc.2009.07.003 PMID: 19713161
25. Marangoni E, Vincent-Salomon A, Auger N, Degeorges A, Assayag F, de Cremoux P, et al. A new model of patient tumor-derived breast cancer xenografts for preclinical assays. Clinical cancer research. 2007; 13(13):3989–98. https://doi.org/10.1158/1078-0432.CCR-07-0078 PMID: 17606733

26. Grinde MT, Skrbo N, Moestue SA, Rødland EA, Borgan E, Kristian A, et al. Interplay of choline metabolites and genes in patient-derived breast cancer xenografts. Breast Cancer Research. 2014; 16(1):1–16. https://doi.org/10.1186/bcr3597 PMID: 24447408

27. Cottu P, Marangoni E, Assayag F, De Cremoux P, Vincent-Salomon A, Guyader C, et al. Modeling of response to endocrine therapy in a panel of human luminal breast cancer xenografts. Breast cancer research and treatment. 2012; 133(2):595–606. https://doi.org/10.1007/s10549-011-1815-5 PMID: 22002565

28. Azizi E, Carr AJ, Plitas G, Cornish AE, Konopacki C, Prabhakaran S, et al. Single-cell map of diverse immune phenotypes in the breast tumor microenvironment. Cell. 2018; 174(5):1293–308. e36. https://doi.org/10.1016/j.cell.2018.05.060 PMID: 29961579

29. Yu M, Bardia A, Aceto N, Bersani F, Madden MW, Donaldson MC, et al. Ex vivo culture of circulating breast tumor cells for individualized testing of drug susceptibility. science. 2014; 345(6193):216–20.

30. Sarioglu AF, Aceto N, Kojic N, Donaldson MC, Zeinali M, Hamza B, et al. A microfluidic device for label-free, physical capture of circulating tumor cell clusters. Nature methods. 2015; 12(7):685–91. https://doi.org/10.1038/nmeth.3404 PMID: 25984697

31. Jordan NV, Bardia A, Wittner BS, Benes C, Ligorio M, Zheng Y, et al. HER2 expression identifies dynamic functional states within circulating breast cancer cells. Nature. 2016; 537(7618):102–6. https://doi.org/10.1038/nature19328 PMID: 27556950

32. Szczerba BM, Castro-Giner F, Vetter M, Krol I, Gkountela S, Landin J, et al. Neutrophils escort circulating tumour cells to enable cell cycle progression. Nature. 2019; 566(7745):553–7. https://doi.org/10.1038/s41586-019-0915-y PMID: 30728496

33. Gkountela S, Castro-Giner F, Szczerba BM, Vetter M, Landin J, Scherrer R, et al. Circulating tumor cell clustering shapes DNA methylation to enable metastasis seeding. Cell. 2019; 176(1–2):98–112. e14. https://doi.org/10.1016/j.cell.2018.11.046 PMID: 30633912

34. Aceto N, Bardia A, Miyamoto DT, Donaldson MC, Wittner BS, Spencer JA, et al. Circulating tumor cell clusters are oligoclonal precursors of breast cancer metastasis. Cell. 2014; 158(5):1110–22. https://doi.org/10.1016/j.cell.2014.07.013 PMID: 25171411

35. Cheng Y-H, Chen Y-C, Lin E, Brien R, Jung S, Chen Y-T, et al. Hydro-Seq enables contamination-free high-throughput single-cell RNA-sequencing for circulating tumor cells. Nature communications. 2019; 10(1):1–11.

36. Aceto N, Bardia A, Wittner BS, Donaldson MC, O'Keefe R, Engstrom A, et al. AR expression in breast cancer CTCs associates with bone metastases. Molecular Cancer Research. 2018; 16(4):720–7. https://doi.org/10.1158/1541-7786.MCR-17-0480 PMID: 29453314

37. Iyer A, Gupta K, Sharma S, Hari K, Lee YF, Ramalingam N, et al. Integrative analysis and machine learning based characterization of single circulating tumor cells. Journal of clinical medicine. 2020; 9 (4):1206. https://doi.org/10.3390/jcm9041206 PMID: 32331451

38. Srivastava D, Iyer A, Kumar V, Sengupta D. CellAtlasSearch: a scalable search engine for single cells. Nucleic acids research. 2018; 46(W1):W141–W7. https://doi.org/10.1093/nar/gky421 PMID: 29788498

39. Ghannoum S, Netto WL, Fantini D, Ragan-Kelley B, Parizadeh A, Jonasson E, et al. DIscBIO: a user-friendly pipeline for biomarker discovery in single-cell transcriptomics. International journal of molecular sciences. 2021; 22(3):1399. https://doi.org/10.3390/ijms22031399 PMID: 33573289

40. Burrill DR, Silver PA. Making cellular memories. Cell. 2010; 140(1):13–8. https://doi.org/10.1016/j.cell.2009.12.034 PMID: 20085698

41. Zibara K, Awada Z, Dib L, El-Saghir J, Al-Ghadban S, Ibrik A, et al. Anti-angiogenesis therapy and gap junction inhibition reduce MDA-MB-231 breast cancer cell invasion and metastasis in vitro and in vivo. Scientific reports. 2015; 5(1):1–16. https://doi.org/10.1038/srep12598 PMID: 26218768

42. Okumura M, Yamamoto M, Sakuma H, Kojima T, Maruyama T, Jamali M, et al. Leptin and high glucose stimulate cell proliferation in MCF-7 human breast cancer cells: reciprocal involvement of PKC-α and PPAR expression. Biochimica et Biophysica Acta (BBA)-Molecular Cell Research. 2002; 1592(2):107–16.

43. Fang M, Shen Z, Huang S, Zhao L, Chen S, Mak TW, et al. The ER UDPase ENTPD5 promotes protein N-glycosylation, the Warburg effect, and proliferation in the PTEN pathway. Cell. 2010; 143(5):711–24. https://doi.org/10.1016/j.cell.2010.10.010 PMID: 21074248

44. Duncan OD. The measurement of population distribution. Population Studies. 1957; 11(1):27–45.

45. Myint AZ, Tun KMM. Grid-Based Spatial Index Method for Location-Based Nearest Neighbour Search. International Journal of Future Computer and Communication. 2020; 9(2).

46. Nunes L, Pessoa M, Araujo A, Sousa R, Silva J, Leite L, et al. Characterization of edaphic fauna in different monocultures in Savanna of Piauí. Brazilian Journal of Biology. 2020; 81:657–64.

47. Del Monte U. Does the cell number 109 still really fit one gram of tumor tissue? Cell cycle. 2009; 8 (3):505–6. https://doi.org/10.4161/cc.8.3.7608 PMID: 19176997

48. Makhoul C, Gosavi P, Duffield R, Delbridge B, Williamson NA, Gleeson PA. Intersectin-1 interacts with the golgin GCC88 to couple the actin network and Golgi architecture. Molecular biology of the cell. 2019; 30(3):370–86. https://doi.org/10.1091/mbc.E18-05-0313 PMID: 30540523

49. Capaci V, Bascetta L, Fantuz M, Beznoussenko GV, Sommaggio R, Cancila V, et al. Mutant p53 induces Golgi tubulo-vesiculation driving a prometastatic secretome. Nature communications. 2020; 11 (1):1–19.

50. Kellokumpu S, Sormunen R, Kellokumpu I. Abnormal glycosylation and altered Golgi structure in colorectal cancer: dependence on intra-Golgi pH. FEBS letters. 2002; 516(1–3):217–24. https://doi.org/10.1016/s0014-5793(02)02535-8 PMID: 11959136

51. Manca S, Frisbie CP, LaGrange CA, Casey CA, Riethoven J-JM, Petrosyan A. The role of alcohol-induced Golgi fragmentation for androgen receptor signaling in prostate cancer. Molecular Cancer Research. 2019; 17(1):225–37. https://doi.org/10.1158/1541-7786.MCR-18-0577 PMID: 30224543

52. Győrffy B, Lanczky A, Eklund AC, Denkert C, Budczies J, Li Q, et al. An online survival analysis tool to rapidly assess the effect of 22,277 genes on breast cancer prognosis using microarray data of 1,809 patients. Breast cancer research and treatment. 2010; 123(3):725–31. https://doi.org/10.1007/s10549-009-0674-9 PMID: 20020197

53. Lánczky A, Győrffy B. Web-based survival analysis tool tailored for medical research (KMplot): development and implementation. Journal of Medical Internet Research. 2021; 23(7):e27633. https://doi.org/10.2196/27633 PMID: 34309564

54. Benzekry S, Lamont C, Beheshti A, Tracz A, Ebos JM, Hlatky L, et al. Classical mathematical models for description and prediction of experimental tumor growth. PLoS Comput Biol. 2014; 10(8):e1003800. https://doi.org/10.1371/journal.pcbi.1003800 PMID: 25167199

55. Byrne HM. Dissecting cancer through mathematics: from the cell to the animal model. Nature Reviews Cancer. 2010; 10(3):221–30. https://doi.org/10.1038/nrc2808 PMID: 20179714

56. Liotta LA, Saidel GM, Kleinerman J. Stochastic model of metastases formation. Biometrics. 1976:535–50. PMID: 963169

57. Iwata K, Kawasaki K, Shigesada N. A dynamical model for the growth and size distribution of multiple metastatic tumors. Journal of theoretical biology. 2000; 203(2):177–86. https://doi.org/10.1006/jtbi.2000.1075 PMID: 10704301

58. Cook LM, Araujo A, Pow-Sang JM, Budzevich MM, Basanta D, Lynch CC. Predictive computational modeling to define effective treatment strategies for bone metastatic prostate cancer. Scientific reports. 2016; 6(1):1–12.

59. Strobl MA, West J, Viossat Y, Damaghi M, Robertson-Tessi M, Brown JS, et al. Turnover modulates the need for a cost of resistance in adaptive therapy. Cancer Research. 2021; 81(4):1135–47. https://doi.org/10.1158/0008-5472.CAN-20-0806 PMID: 33172930

60. Yankeelov TE, Atuegwu N, Hormuth D, Weis JA, Barnes SL, Miga MI, et al. Clinically relevant modeling of tumor growth and treatment response. Science translational medicine. 2013; 5(187):187ps9–ps9. https://doi.org/10.1126/scitranslmed.3005686 PMID: 23720579

61. Alfonso J, Köhn-Luque A, Stylianopoulos T, Feuerhake F, Deutsch A, Hatzikirou H. Why one-size-fits-all vaso-modulatory interventions fail to control glioma invasion: in silico insights. Scientific reports. 2016; 6(1):1–15.

62. Bisel B, Wang Y, Wei J-H, Xiang Y, Tang D, Miron-Mendoza M, et al. ERK regulates Golgi and centrosome orientation towards the leading edge through GRASP65. The Journal of cell biology. 2008; 182 (5):837–43. https://doi.org/10.1083/jcb.200805045 PMID: 18762583

63. Ghaffari Laleh N, Loeffler CML, Grajek J, Staňková K, Pearson AT, Muti HS, et al. Classical mathematical models for prediction of response to chemotherapy and immunotherapy. PLOS Computational Biology. 2022; 18(2):e1009822. https://doi.org/10.1371/journal.pcbi.1009822 PMID: 35120124

64. Lai X, Geier OM, Fleischer T, Garred Ø, Borgen E, Funke SW, et al. Toward personalized computer simulation of breast cancer treatment: A multiscale pharmacokinetic and pharmacodynamic model informed by multitype patient data. Cancer research. 2019; 79(16):4293–304. https://doi.org/10.1158/0008-5472.CAN-18-1804 PMID: 31118201

65. DiMilla PA, Barbee K, Lauffenburger DA. Mathematical model for the effects of adhesion and mechanics on cell migration speed. Biophysical journal. 1991; 60(1):15–37. https://doi.org/10.1016/S0006-3495(91)82027-6 PMID: 1883934

66. Swanson KR, Bridge C, Murray J, Alvord EC Jr. Virtual and real brain tumors: using mathematical modeling to quantify glioma growth and invasion. Journal of the neurological sciences. 2003; 216(1):1–10. https://doi.org/10.1016/j.jns.2003.06.001 PMID: 14607296

67. Hatzikirou H, Deutsch A. Cellular automata as microscopic models of cell migration in heterogeneous environments. Current topics in developmental biology. 2008; 81:401–34. https://doi.org/10.1016/S0070-2153(07)81014-3 PMID: 18023736

68. Cao Y, Ghabache E, Miao Y, Niman C, Hakozaki H, Reck-Peterson SL, et al. A minimal computational model for three-dimensional cell migration. Journal of the Royal Society Interface. 2019; 16 (161):20190619. https://doi.org/10.1098/rsif.2019.0619 PMID: 31847757

69. Metzcar J, Wang Y, Heiland R, Macklin P. A review of cell-based computational modeling in cancer biology. JCO clinical cancer informatics. 2019; 2:1–13. https://doi.org/10.1200/CCI.18.00069 PMID: 30715927

70. Hsu C-Y, Wang C-W, Kuo C-C, Chen Y-H, Lan K-H, Cheng A-L, et al. Tumor compactness improves the preoperative volumetry-based prediction of the pathological complete response of rectal cancer after preoperative concurrent chemoradiotherapy. Oncotarget. 2017; 8(5):7921. https://doi.org/10.18632/oncotarget.13855 PMID: 27974702

71. Joshi G, Chi Y, Huang Z, Wang Y. Aβ-induced Golgi fragmentation in Alzheimer's disease enhances Aβ production. Proceedings of the National Academy of Sciences. 2014; 111(13):E1230–E9.